nature astronomy

LETTERS

PUBLISHED: 12 DECEMBER 2016 | VOLUME: 1 | ARTICLE NUMBER: 0001

Terahertz and far-infrared windows opened at Dome A in Antarctica

Sheng-Cai Shi[1]*, Scott Paine[2], Qi-Jun Yao[1], Zhen-Hui Lin[1], Xin-Xing Li[1,†], Wen-Ying Duan[1], Hiroshi Matsuo[3], Qizhou Zhang[2], Ji Yang[1], M. C. B. Ashley[4], Zhaohui Shang[5,7] and Zhong-Wen Hu[6]

The terahertz and far-infrared band, ranging from approximately 0.3 THz to 15 THz (1 mm to 20 μm), is important for astrophysics as it hosts the peak of the thermal radiation of the cold component of the Universe as well as many spectral lines that trace the cycle of interstellar matter[1–8]. However, water vapour makes the terrestrial atmosphere opaque to this frequency band over nearly all of the Earth's surface[9]. Early radiometric measurements[10] below 1 THz at Dome A (80° 22′ S, 77° 21′ E), the highest point of the cold and dry Antarctic ice sheet, suggest that this site may offer the best possible access for ground-based astronomical observations in the terahertz and far-infrared band. To fully assess the site conditions and to address the uncertainties in radiative transfer modelling of the atmosphere, we carried out measurements of atmospheric radiation from Dome A with a Fourier transform spectrometer, spanning the entire water vapour pure rotation band from 20 μm to 350 μm. Our measurements reveal substantial transmission in atmospheric windows throughout the whole band. By combining our broadband spectra with data on the atmospheric state over Dome A, we set new constraints on the spectral absorption of water vapour at upper tropospheric temperatures, which is important for accurate modelling of the terrestrial climate. We find that current spectral models significantly underestimate the H_2O continuum absorption.

We directly measured the zenith atmospheric radiation at Dome A throughout the H_2O pure rotation band, that is, the terahertz and far-infrared (FIR) band. This study was made possible by China's ongoing development of Dome A as a scientific base including facilities for astronomy[10,11]. Such broadband measurements have not been made before at this site and are needed because narrowband radiometry combined with modelling is insufficient for the accurate evaluation of the broadband transmission, primarily due to limited understanding of the H_2O continuum absorption, especially at the low temperatures typical of Dome A. Ground-based measurements are needed because satellite measurements have inadequate sensitivity in the lower troposphere. Our results were obtained with a remotely operated Fourier transform spectrometer (FTS)[12], which was deployed to Dome A by the 26th Chinese Antarctic Research Expedition (CHINARE) team during the 2009/2010 traverse. The FTS ran for 19 months from January 2010 until August 2011, measuring the downwelling zenith sky radiance from 0.75 THz to 15 THz with a spectral resolution of 13.8 GHz. Technical details regarding the instrument and calibration methods are given in Methods. As discussed there, to achieve sufficient signal-to-noise ratios, the spectra were averaged into 6-hour bins, and a good calibration for radiance was achieved at frequencies above 1 THz.

For the site survey statistics, we derived transmittance spectra from the measured radiance spectra using the isothermal radiative transfer approximation described in Methods. The fractional accuracy of the transmittance thus obtained corresponds to the fractional change in the absolute atmospheric temperature across the scale height of the water vapour column, which is approximately 5%. Transmittance errors associated with strong water lines terminating within the instrument or in the surface boundary layer can be recognized by their correspondence to the well-known positions of these lines. The key advantage of the isothermal transmittance approximation, in contrast to the more detailed spectroscopic study below, is that it requires no assumptions regarding the vertical structure of the atmosphere.

The transmittance statistics are presented in Fig. 1, where we show quartile transmittance spectra for the entire year (Fig. 1a,c), and for winter (April to September) only (Fig. 1b,d). To correct for uneven sampling over the calendar year, when compiling percentile statistics we applied a de-biasing procedure whereby spectra obtained in calendar periods that were sampled only once during the two years of operation were duplicated, and brief gaps in sampling were covered by interpolating between temporally adjacent spectra. Sufficiently high transmittance to support astronomical observation (~20%) is consistently observed in winter in the three windows at 1.03, 1.3 and 1.5 THz, which encompass the astrophysically important spectral lines indicated in Fig. 1. Much higher FIR transmittance (>40%) is found in a number of windows starting at 7.1 THz. Although our spectra are limited to frequencies above 1 THz, they are consistent with Dome A being an excellent year-round observing site in the submillimetre windows below 1 THz. Moreover, the extremely dry conditions that open the windows above 1 THz at Dome A occur during a much greater time fraction than at other sites where observations in these windows can be attempted[5,13,14].

Given the plans for future observatories and scientific facilities at Dome A, the exposed terahertz and FIR windows present a unique opportunity for ground-based astronomy. For example, unique terahertz spectral line transitions from atomic and molecular species such as N^+ at 1.46 THz (205 μm), H_2D^+ at 1.37 THz (219 μm), high-J CO lines and C^+ at a moderate redshift from its rest frequency of 1.90 THz (158 μm) can be observed to trace the lifecycle

[1]Purple Mountain Observatory, Key Laboratory of Radio Astronomy, Chinese Academy of Sciences, Nanjing 210008, China. [2]Smithsonian Astrophysical Observatory, Cambridge 02138, Massachusetts, USA. [3]National Astronomical Observatory of Japan, Mitaka, Tokyo 181-8588, Japan. [4]The University of New South Wales, Sydney 2052, Australia. [5]Tianjin Normal University, Tianjin 300386, China. [6]Nanjing Institute of Astronomical Optics and Technology, National Astronomical Observatories, Chinese Academy of Sciences, Nanjing 210042, China. [7]National Astronomical Observatories, Chinese Academy of Sciences, Beijing 100012, China. †Present address: Suzhou Institute of Nano-Tech and Nano-Bionics, Chinese Academy of Sciences, Suzhou 215123, China. *e-mail: scshi@pmo.ac.cn

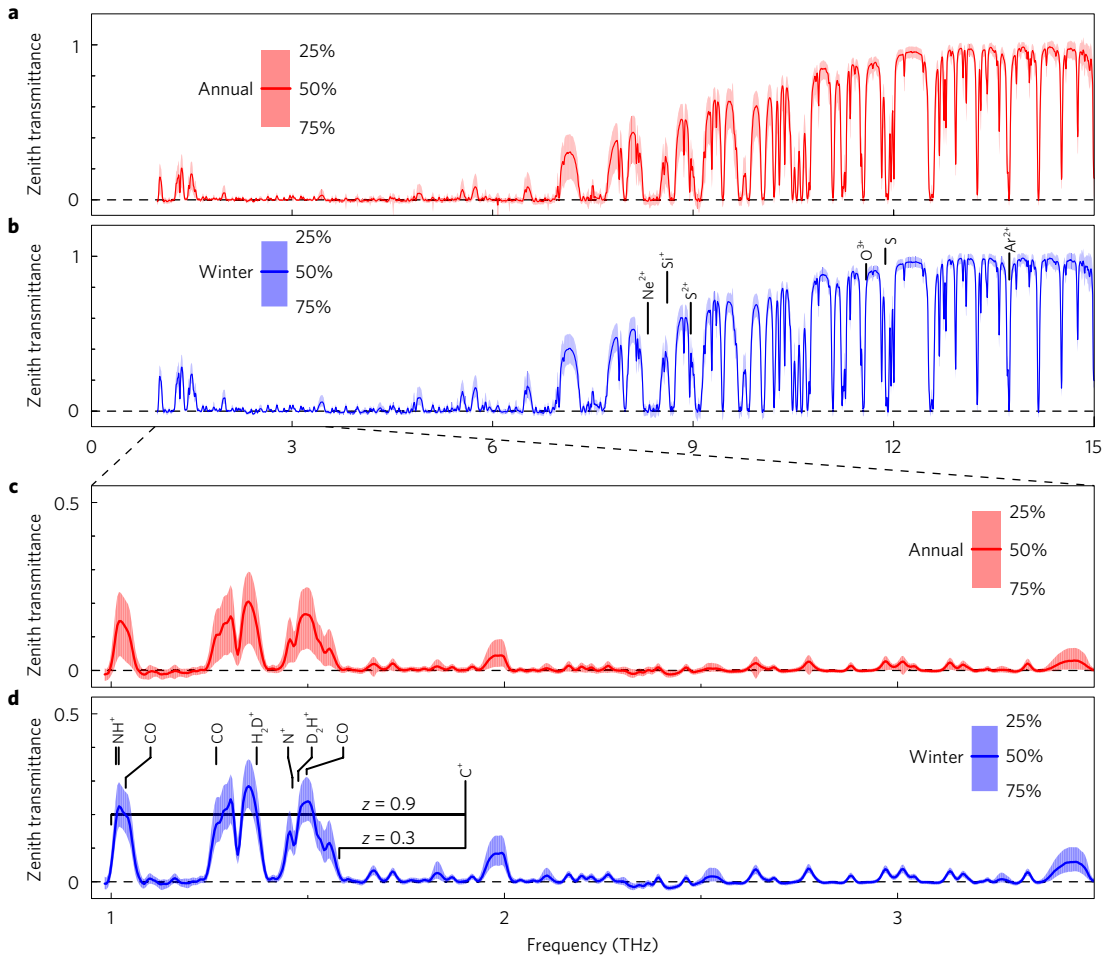

Figure 1 | Zenith atmospheric transmittance spectra measured at Dome A, Antarctica, during 2010–2011. a–d, Spectra are shown for the entire year (**a**,**c**) and for winter (April–September) only (**b**,**d**). Quartile statistics for each frequency channel were compiled independently. Solid lines indicate the median transmittances, and the shaded regions show the interquartile ranges. To account for irregular time sampling throughout the year, data were de-biased as described in the text. Frequencies of several astrophysically important spectral lines are indicated; note that some of these lines are observable only at certain non-zero redshift values *z*.

of stars and interstellar matter, as well as chains of chemical reactions that ultimately shape the chemical composition of planetary systems like our own. In addition, spectral lines of species such as O^{3+} at frequencies greater than 7 THz allow the exploration of the energy balance in the interstellar medium. As a ground-based site, Dome A could support larger facilities, either single telescopes with a large aperture or multiple telescopes phased up as interferometers, with more rapid and agile development cycles than space-based or aircraft-based platforms.

Our measurements also allow us to address an issue in atmospheric science relating to uncertainties in the absorption spectrum of water vapour. These uncertainties are associated with poorly understood collisional effects that give rise to smoothly varying continuum absorption[15,16], which has a significant impact on atmospheric radiation models[17–20]. The importance of measuring the continuum absorption has motivated several recent field experiments, including the Radiative Heating in Underexplored Bands Campaigns[21–23], Earth Cooling by Water Vapor Radiation[24,25] and Continuum Absorption of Visible and IR radiation and its Atmospheric Relevance[26]. However, the full atmospheric temperature range has not been adequately explored. The water vapour continuum absorption includes a component that is associated with homogeneous H_2O–H_2O collisions (known as the self-continuum) that dominates in the warm and humid lower troposphere, and a component associated with heterogeneous collisions (known as the foreign continuum) that dominates in the cold and dry upper troposphere. The measurements we report here from Dome A provide new constraints on the H_2O foreign continuum towards the low range of atmospheric temperatures. In addition, the low H_2O column density over Dome A gives unprecedented access to wavelengths in the core of the H_2O rotation band where previous measurements have lacked sensitivity.

We studied the water vapour absorption spectrum by combining our broadband spectra with auxiliary data on the atmospheric state over Dome A. Given the atmospheric state in the form of vertical profiles of temperature and water vapour concentration over the site, a radiative transfer model can be used to predict the observed radiance spectrum and thereby test the spectral absorption data used in the model. With the exception of the H_2O foreign continuum absorption, the spectral absorption data used in the radiative transfer model are well constrained by laboratory measurements. Therefore, the residuals between the measured and modelled spectra can be interpreted in terms of an implied correction to the continuum absorption coefficient. The radiative transfer model employed the MT_CKD (v. 2.5.2) water vapour continuum[16]. We chose MT_CKD as the reference continuum model for this study because it has been extensively validated in laboratory and field experiments, albeit at higher temperatures than those accessed in this study, and because it is widely used in the atmospheric radiation codes incorporated into climate models.

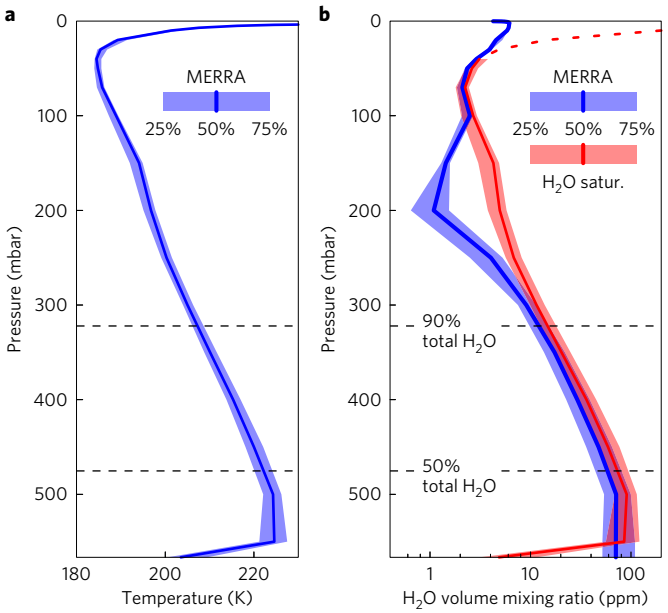

Figure 2 | Atmospheric profiles over Dome A, Antarctica, during the August 2010 study period. a,**b**, Median vertical profiles of temperature (**a**) and H_2O volume mixing ratio (**b**) during August 2010, derived from the NASA MERRA reanalysis[27], are plotted against pressure. The temperature point at the surface, associated with the strong winter surface inversion, is from our own instrument. The H_2O volume mixing ratio is relative to the total gas density. The shading around the median profiles indicates the interquartile range of variation during the month. For comparison with the MERRA water vapour profile, the red profile in **b** shows the saturated mixing ratio over ice that corresponds to the MERRA temperature profile and its interquartile variation. The horizontal dotted lines indicate pressures below which the median MERRA H_2O profile contains 90% and 50% of the total H_2O column density, indicating the small range in temperature across most of the H_2O column. The column density-weighted mean H_2O temperature for the study period was 218 K.

Our starting point for estimating the atmospheric state was the NASA Modern-Era Retrospective Analysis for Research and Applications (MERRA) reanalysis[27] interpolated over Dome A. MERRA provides an estimate of the global atmospheric state constrained by satellite, surface, and upper air measurements with a 6-hour resolution matching the temporal averaging bins of our spectra. The ranges of MERRA-derived vertical temperature and water vapour profiles during the period of this study (August 2010) are shown in Fig. 2. The modest interquartile variation observed in these profiles, together with relatively high data quality in our spectra, are the reasons we decided to focus on this period. Recent dropsonde validations[28] of the satellite-derived temperature profiles over Antarctica give us high confidence in the data that constrain the MERRA temperature profiles. Moreover, as expected, the lower part of the MERRA water vapour profile closely tracks the ice saturation vapour pressure profile. As indicated in Fig. 2, the temperature range across the water vapour column was small during the study period.

MERRA does not resolve the strong winter Antarctic surface inversion[29], and the absolute accuracy of the MERRA water vapour profile is uncertain. We therefore used an analysis method that involved dividing the measured spectral interval into two parts: the band-edge frequencies ($f < 3.6$ THz and $f > 12.5$ THz) that comprise spectral channels where the observed radiance is insensitive to the continuum, and the mid-band frequencies (3.6 THz $< f <$ 12.5 THz) where the radiance in the transmission windows includes a significant continuum contribution. The band-edge channels were used with a radiative transfer model[30] to fit a two-parameter adjustment to the initial MERRA-derived profiles. These two parameters were a scaling factor on the MERRA water vapour profile in the troposphere and the base temperature of a surface layer modelling the surface inversion.

An example of one of these fits is shown in Fig. 3a. With the atmospheric state anchored to the band-edge channels, we found that the radiances in the mid-band windows were consistently underestimated. Using the channel-by-channel derivative of the model radiance with respect to the foreign continuum absorption coefficient, the residuals in the windows were used to derive an implied adjustment to the absorption coefficient. Figure 3b compares the MT_CKD absorption coefficient with the quartile statistics of the adjusted values found for all of the spectra included in this study, which cover a range of water vapour column densities from 70 μm to 220 μm precipitable water vapour. The consistent value found for the adjusted foreign continuum absorption coefficient across this wide range of water vapour column densities, particularly in the higher signal-to-noise windows from 5 THz to 9 THz, is strong evidence that the residuals are indeed associated with water vapour absorption as opposed to systematic calibration errors, errors in the dry air spectroscopy or absorption by other atmospheric constituents such as hydrometeors. The smooth trend in the adjusted continuum, as well as the generally good fit near the centre of unsaturated water lines, would also appear to rule out errors in the H_2O line-by-line spectroscopy as the origin of the radiance residuals. The implied adjustment to the MT_CKD foreign continuum absorption coefficient at the column density-weighted mean H_2O temperature of 218 K over these spectra was as high as a factor of 2.5 in the mid-band windows just below 9 THz.

By reaching new extremes of low temperature and accessing windows in the core of the H_2O pure rotation band, our measurements at Dome A have provided new constraints on the spectral absorption of water vapour that are important for modelling radiative processes in the cold upper troposphere and for retrieving atmospheric properties from outbound spectral radiance measurements. Taken together with the transmittance statistics for the astronomical observing windows discussed above, our measurements demonstrate the value of this unique site to both astronomy and atmospheric science.

Methods

Description of the instrument. The Dome A FTS is a polarizing Michelson (Martin–Puplett) interferometer[31]. The conceptual and optical designs were developed at the Purple Mountain Observatory and the Smithsonian Astrophysical Observatory, and descriptions of the designs are available[12]. Detailed engineering and fabrication of the interferometer, detectors and band-defining filters were carried out by Blue Sky Spectroscopy and QMC Instruments. Photographs of the instrument and its installation at Dome A in the University of New South Wales PLATeau Observatory (PLATO) support module[32] are presented in Supplementary Fig. 1.

At Dome A the instrument was required to run unattended on low power, placing significant constraints on detector sensitivity and calibration. The use of cryogenically cooled low-noise detectors that are typically employed in similar instruments to achieve background-limited sensitivity was not feasible, and instead the instrument used DLATGS (deuterated L-alpha-alanine doped triglycine sulfate) pyroelectric detectors operated at ambient temperature.
Actively cooled or heated black-body loads for calibration were also not practical within the instrument power budget. Instead, calibration was accomplished using two passive loads. These were an internal warm reference load terminating one of the interferometer input ports and an outdoor cold calibration load on the roof of PLATO, which could swing under computer control to intercept the view towards the zenith sky. Supplementary Fig. 2 shows a plot of the time history of these two load temperatures over the course of the campaign. The typical temperature difference available for calibration was approximately 40 K in summer and 50 K in winter. The loads were made using the radiation-absorbent material TKRAM, a product of Thomas Keating Ltd, with a power reflectivity of less than 1% at terahertz frequencies.

The spectral coverage of the FTS (750 GHz–15 THz) was split into two bands defined by different low-pass filters in front of the detector at each of the two output ports of the interferometer. The high band admitted all power up to

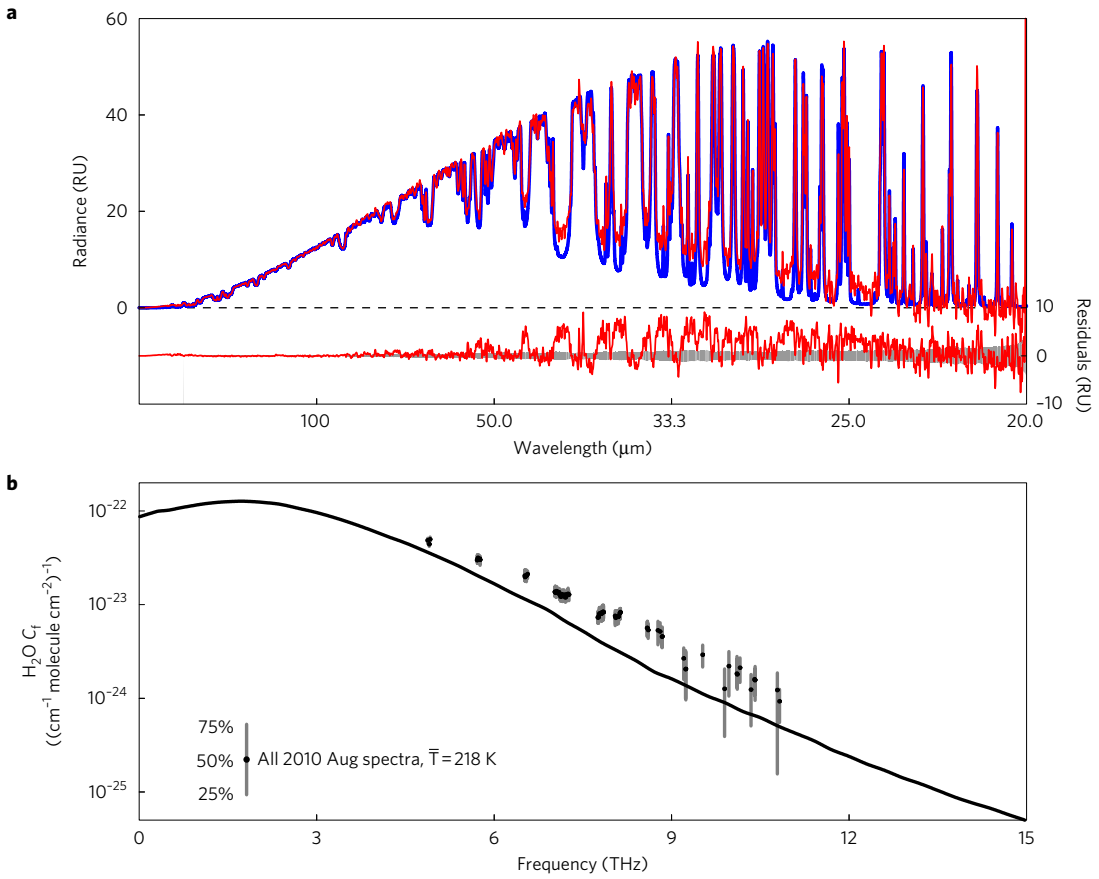

Figure 3 | H_2O foreign continuum correction derived from spectral residuals. a, An example of a spectral fit from the August 2010 data set. The measured radiance spectrum is shown in red, and the model spectrum computed from the scaled MERRA profiles is shown in blue. Note the significant residuals in the spectral windows within the H_2O rotation band; the grey band plotted along with the residuals indicates the noise level in the measured spectrum (measured 8 August 2010, 0–6 UT). **b**, Quartile statistics (symbols) of the adjusted H_2O foreign continuum absorption coefficient (C_f) derived from the radiance residuals for all August 2010 spectra at 218 K compared with the MT_CKD v. 2.5.2 water vapour continuum model (solid line). The channels used in this analysis were screened using the criteria described in Methods. The units of C_f are those customarily used in the literature[16,25,26], and refer to the continuum absorption at a reference temperature $T_0 = 296$ K and foreign gas partial pressure $P_0 = 1{,}013$ mbar. The H_2O foreign continuum contribution τ_f to the optical depth through a column of water vapour with a column density N_{H_2O}(molecule cm^{-2}) at temperature T and foreign gas pressure P is $\tau_f = C_f N_{H_2O}(P / P_0)(T_0 / T) \times \nu \tanh(hc\nu / 2kT)$, where the frequency ν is in wavenumber units (cm^{-1}). RU corresponds to mW m^{-2} (cm^{-1})$^{-1}$ sr^{-1}.

15 THz, while the low band was restricted to frequencies below 3.6 THz. This allowed the low band detector to operate at increased optical throughput, and also reduced radiative background noise due to the steeply increasing Planck radiance and associated atmospheric brightness fluctuations towards higher frequencies. The 750 GHz low-frequency coverage limit of the FTS was determined by the signal-to-noise ratio achieved in the low band given the sensitivity of the FTS combined with the temporal stability of the atmosphere. The 15 THz high frequency limit was selected to substantially cover the H_2O pure rotation band and was high enough to include several optically thin windows and unsaturated H_2O emission lines.

The spectral resolution was set by the interferometer scan length and the weighting applied for apodization. The scan length was ±12.5 mm relative to the zero path difference (ZPD) position of the interferometer, and a Blackman weighting function was applied in processing. This yielded an instrumental resolution function with a full width at half maximum of 13.8 GHz, chosen to be narrow enough to isolate a number of unsaturated H_2O lines, but broad enough to increase optical throughput and channel bandwidth given the other constraints on sensitivity noted above. This resolution was sufficiently narrow to have a minimal effect on the window transmittances measured by the isothermal method, and the instrument resolution function was included in the radiative transfer model used for the continuum absorption study.

Spectral calibration and averaging. At Dome A, each scan of the interferometer took 25 s. Interferograms were stored as eight integrated scans, alternately viewing the zenith sky and the external passive calibration load after each integration. A complete measurement cycle comprising one integration on the sky and one on the calibration load thus took approximately 9 min. Each sky/load pair of interferograms (for each of the two detector bands) was Fourier-transformed and processed to yield calibrated spectra using a complex domain calibration method similar to a previously described method[33]. Below, we describe the calibration of a single detector band. In processing, the spectra for the two bands were combined in a channel-by-channel noise-weighted average to produce a single merged spectrum for each sky/load measurement cycle.

An important factor in the calibration is that both the sky and the outside calibration load were viewed through a 2-mm-thick high-density polyethylene (HDPE) window at the top of a tube that passed through the insulated roof of the PLATO module; the window absorption and reflection thus needed to be accounted for. The window, located directly below the calibration load, was tilted to avoid interference effects and to direct the reflected view on to absorbent material lining the tube. The bottom of the tube was covered with a thin polyethylene membrane with negligible optical reflection and absorption that prevented convective heat transfer to the interior of PLATO so that the temperature of the window and upper end of the tube would follow the outdoor temperature. We therefore assumed that the window absorption and reflection were terminated at the outside calibration load temperature.

Under this assumption, during the calibration phase when the two input ports of the interferometer viewed the reference load and the calibration load, the raw spectrum obtained by complex Fourier transformation of the interferogram can be written as:

$$S_{cal}(\nu) = R_c(\nu) \times (B_\nu(T_{cc}) - B_\nu(T_{rc})) \quad (1)$$

where R_c is the complex responsivity of the FTS during the calibration phase, $B_\nu(T_{cc})$ is the Planck radiance at the temperature T_{cc} of the calibration load during the calibration phase of the measurement cycle and $B_\nu(T_{rc})$ is the Planck radiance at the temperature T_{rc} of the reference load during the calibration cycle.

During the on-sky phase of the measurement cycle, the raw spectrum is:

$$S_{sky}(\nu) = R_s(\nu) \times [\mathcal{T}_w(\nu) I_{sky}(\nu) + (1 - \mathcal{T}_w(\nu)) B_\nu(T_{cs}) - B_\nu(T_{rs})] \quad (2)$$

where

$$\mathcal{T}_w(\nu) = (1-r)^2 [1 - a(\nu)] \quad (3)$$

is the net window transmittance approximated as the product of two surface reflections at a frequency-independent power reflectivity r and a frequency-dependent single-pass absorption $a(\nu)$. $I_{sky}(\nu)$ is the downwelling zenith radiance and $B_\nu(T_{cs})$ and $B_\nu(T_{rs})$ are the Planck radiances at the calibration load and reference load temperatures, respectively, during the sky viewing phase of the measurement cycle.

We expect the complex responsivities R_c and R_s to be identical apart from a linear phase term that is associated with any drift δ_{ZPD} in the ZPD position of the interferometer. That is,

$$R_s(\nu) = R_c(\nu) e^{2\pi i (\delta_{ZPD} \times \nu / c)} \quad (4)$$

If we assume $\delta_{ZPD} = 0$, then the complex responsivities cancel in forming the ratio $S_{sky}(\nu)/S_{cal}(\nu)$, and the calibration equation for the FTS can be written as:

$$I_{diff}(\nu) = I_{sky}(\nu) - I_{cc}(\nu) = \left(\frac{S_{sky}(\nu)}{S_{cal}(\nu)} - 1 \right) \times I_0(\nu) - \Delta I(\nu) \quad (5)$$

where

$$I_0(\nu) = \frac{1}{\mathcal{T}_w(\nu)} (B_\nu(T_{cc}) - B_\nu(T_{rc})) \quad (6)$$

is the (typically negative) difference in load radiances, adjusted for the window transmittance, and

$$\Delta I(\nu) = \frac{1 - \mathcal{T}_w(\nu)}{\mathcal{T}_w(\nu)} (B_\nu(T_{cs}) - B_\nu(T_{cc})) - \frac{1}{\mathcal{T}_w(\nu)} (B_\nu(T_{rs}) - B_\nu(T_{rc})) \quad (7)$$

is a much smaller term associated with changes in the load temperature between the calibration and sky phases of a measurement cycle. Note that the effect of forming the ratio of the complex spectra $S_{sky}(\nu)$ and $S_{cal}(\nu)$ is to cancel out the phase in the complex responsivity, so that the real part $\mathrm{Re}(I_{diff}(\nu))$ consists of the calibrated radiance difference between the zenith sky and calibration load plus a noise component, and the imaginary part $\mathrm{Im}(I_{diff}(\nu))$ consists of noise only. To estimate the noise variance in each channel of the spectrum $\mathrm{Re}(I_{diff}(\nu))$, we applied bidirectional exponential smoothing to $|\mathrm{Im}(I_{diff}(\nu))|^2$, with a $1/e$ width of ± 5 channels. This noise variance is used to optimally weight the channel-by-channel combination of the two spectral bands of the FTS into the single merged spectrum for each measurement cycle, and to optimally weight the subsequent averages of multiple spectra into 6-hour integrations.

The effect of a small ZPD drift ($\delta_{ZPD} \ll \lambda$) is a small rotation in the complex plane of the ratio spectrum $S_{sky}(\nu)/S_{cal}(\nu)$, projecting part of the real signal component onto the imaginary noise component. This would produce an undesirable bias in our noise estimates. To avoid this, we computed an estimate of δ_{ZPD} for each frequency channel in the highest signal-to-noise ratio part of the high-band ratio spectrum, from 10 THz to 14 THz, averaged these into a single estimate for δ_{ZPD} for the spectrum, and applied a corresponding phase correction to the ratio $S_{sky}(\nu)/S_{cal}(\nu)$ for both the high and low band spectra. The cumulative distribution (Supplementary Fig. 3) of these estimates over all of the sky/calibration cycles in the campaign showed that δ_{ZPD} was typically less than 1 μm, much smaller than the shortest wavelength of operation $\lambda_{min} = 20$ μm. Ideally, δ_{ZPD} should have a median of zero if it is associated with bounded temperature variations, and indeed the actual median was $\bar{\delta}_{ZPD} = -0.03$ μm, which is negligible.

In the FTS instrument several factors can potentially contribute to gain errors that multiply $I_{diff}(\nu)$. These include possible thermometry errors associated with temperature gradients across the calibration load between temperature sensors and the absorbing surface, and accumulation or removal of ice or snow particles on the HDPE window between the sky and calibration load viewing phases of the measurement cycle. The presence of several optically thin windows above 12 THz provides the opportunity to make a differential correction for gain errors under the dry conditions that prevail at this site. This correction takes advantage of the approximately linear relationship under optically thin conditions between the average radiance I_1 in a wide transmission window at $\bar{\nu}_1 = 12.25$ THz, and the average radiance I_2 in three narrower windows with average frequency $\bar{\nu}_2 = 13.93$ THz, which is:

$$I_2 = a \times (I_1 - I_2) + b \quad (8)$$

Given an initial calibration, equation (8) can be used to produce a refined estimate of the location of the high-frequency zero-radiance baseline based on the difference between the two near-baseline radiances I_1 and I_2. Because these radiances are already small, the coefficients a and b need not be known with high accuracy. Starting with median climatological profiles based on MERRA, we varied a scale factor on the tropospheric water vapour profile to find the slope $a = 1.53$, and dry intercept $b = 0.31$ mW m^{-2} (cm^{-1})$^{-1}$ sr^{-1}. Given an initial calibrated radiance $I_{diff}(\bar{\nu}_2)$, the gain correction factor η multiplying $I_{diff}(\nu)$ that corrects the high-frequency spectral baseline is:

$$\eta = \frac{I_{diff}(\bar{\nu}_2) - I_2 + b}{I_{diff}(\bar{\nu}_2) - a \times (I_1 - I_2)} \quad (9)$$

The gain correction factor η was computed and applied to the 6-hour averaging bins. In approximately 11% of cases where conditions were not sufficiently dry or stable, no correction was made. For the corrected cases, the cumulative distribution of η (Supplementary Fig. 4) showed that while there was negligible systematic bias in the gain calibration during the August 2010 study period, there was a systematic gain bias of approximately 5% over the entire campaign, possibly due to solar heating of the calibration load during the months when the Sun was up.

The transmittance $\mathcal{T}_w(\nu)$ of the HDPE window was calibrated *in situ* using an iterative method. This was necessary because the absorption spectrum of HDPE has significant temperature dependence[34,35], and could thus be expected to change between normal room temperature and deployment to Dome A. We made an initial estimate of the single-pass absorption $a(\nu)$ based on low-temperature HDPE absorption spectra in the literature[34–36], scaling the loss tangent spectrum (that is, the ratio of the imaginary to real refractive index) to minimize the residuals in an initial model fit to the radiances in high-frequency optically thin windows, where the radiances approach the zero radiance baseline under dry conditions. We then checked and adjusted this initial absorption estimate by linear regression on the isothermally approximated optical depth in the individual transmittance windows within the H_2O rotation band against precipitable water constrained by the unsaturated H_2O lines above the rotation band envelope. The August 2010 subset of the data, which, as mentioned in the main text, had the highest quality and covered the driest period, was used for this analysis. An example of one such regression is shown in Supplementary Fig. 5. The dry intercept of the optical depth is small, and in contrast to the wet absorption, it can be modelled accurately using spectral data (principally for N_2 collision-induced absorption) that are well constrained by laboratory measurements at the relevant temperatures[30]. For each atmospheric window within the H_2O rotation band, we computed an adjustment factor on the HDPE absorption based on the difference between the modelled dry optical depth and the regression intercept.

The adjustment factors were linearly interpolated in frequency between the windows when applied to the HDPE absorption spectrum, and the FTS spectra were then recalibrated. This process was iterated to convergence, which was substantially reached after the first iteration. The initial and final estimates of $a(\nu)$ are plotted in Supplementary Fig. 6. In contrast to the absorption, the real part $n = 1.53$ of the refractive index of HDPE is essentially independent of frequency and temperature over our range of interest, so the accuracy of the reflection loss, that is, $(1-r)^2 = 0.914$, is not a source of significant uncertainty.

The analysis used to calibrate the HDPE window provided an approximate indication of the underestimation of the H_2O continuum absorption coefficient. We compared the regression slope with an estimate from a model based on the monthly average atmospheric state from MERRA with a scaled water vapour profile, as shown in Supplementary Fig. 5. The figure also shows the effect of turning off the H_2O continuum in the model, illustrating the relative contributions of the H_2O continuum and line absorption in the 7.1 THz (42 μm) spectral window. In principle, either the line wing absorption or the continuum absorption could be increased to match the regression slope in any particular window. However, the consistency of the continuum adjustment across multiple windows bordered by H_2O lines with various strengths and frequency separations strongly supports our conclusion that it is the continuum that is underestimated.

Transmittance computation and statistics. As discussed in the main text, the transmittance statistics presented in Fig. 1 were compiled from transmittance spectra derived from the measured zenith radiance spectra using an isothermal atmosphere approximation. This is defined as:

$$t_{iso}(\nu) = \frac{B_\nu(T_{atm}) - I_{sky}(\nu)}{B_\nu(T_{atm}) - B_\nu(T_{cb})} \quad (10)$$

where T_{atm} is the effective temperature of the atmosphere and $B_\nu(T_{atm})$ is the corresponding Planck radiance, and $B_\nu(T_{cb})$ is the Planck radiance corresponding to the cosmic microwave background at $T_{cb} = 2.7$ K. which is insignificant except at our lowest measured frequencies. The celestial diffuse infrared background at higher frequencies is negligible relative to the atmospheric radiance.

As discussed in the main text, the fractional accuracy of the isothermal atmosphere approximation for transmittance over Dome A is expected to be approximately 5%, provided an appropriate value is chosen for T_{atm}. Surface air

temperature is not a good proxy for T_{atm}, particularly in the Antarctic winter when surface inversion depths exceeding 20 K are often observed[29]. Instead, we derive T_{atm} using the opaque channels forming the Planck baseline of the measured radiance spectrum. These channels are terminated over a range of altitudes extending well above any surface inversion that may be present. The baseline is found by converting observed zenith radiance $I_{sky}(\nu)$ in each channel to the equivalent Planck brightness temperature via the inverse Planck function:

$$T_b(\nu) = \frac{h\nu}{k \ln\left(1 + \frac{2h\nu^3}{c^2 I(\nu)}\right)} \quad (11)$$

We then form a histogram weighted by signal-to-noise ratio of the T_b values for all the channels in a spectrum in bins 1 K wide. The temperature at the centre of the bin with the highest weighted count is then taken as the effective T_{atm}. This procedure is illustrated for an example spectrum in Supplementary Fig. 7.

Continuum adjustment statistics. When compiling the statistics of the water vapour continuum absorption coefficient adjustments plotted in Fig. 3 of the main text, we applied several screening criteria to select suitable spectral channels. Only those channels between 3.6 THz and 12.6 THz, that were not used in the fits that constrain the water vapour profile scaling were included in the analysis. Within this frequency range, channels were further screened as described below.

We screened channels for zenith transmittance (based on the fitted model spectrum), requiring transmittance between $t = 0.3$ and $t = 0.9$. The purpose of this screen was to eliminate channels for which the optical depth was too high or too low. Channels with high optical depth are sensitive to the low-level structure of the water vapour and temperature profiles, potentially introducing systematic bias. Channels for which the optical depth is too low have insufficient sensitivity to the absorption coefficient relative to calibration error affecting the radiance baseline. We additionally required that the change in transmittance across the width of a single spectral channel (13.8 GHz) was $\Delta t \leq 0.05$ so that channels in the near wings of the spectral lines would be rejected.

For channels that passed the zenith transmittance screening, we then applied the following statistical screens. First, to ensure meaningful quartile statistics, a channel must have passed the transmittance screen in no fewer than 16 spectra to be included in the analysis. Next, we identified clear spectral windows by requiring at least five adjacent channels to pass this screen. Finally, adjacent channels with median continuum absorption coefficient adjustment factors differing by more than 5% were rejected. This led to the rejection of channels affected by errors in the strength or broadening coefficient of spectral lines bordering the spectral transmission windows, and those with a signal-to-noise ratio insufficient to produce a median estimate less than 5%, noting that the underlying variation in the continuum across the width of a single spectral channel will be much smaller than this.

As a test of the sensitivity of our analysis to the initial MERRA profiles, we repeated the analysis after applying ±2 K perturbations to the MERRA temperature profiles, and after replacing the MERRA water vapour profile with the ice saturation profile in the troposphere, and found that these changes did not significantly affect our results within the noise level of our spectra. This is because our scaling of the MERRA water vapour profile effectively calibrated the mid-band continuum against the band edge line absorption. As discussed above (see also Supplementary Fig. 5), the discrepancy in the continuum absorption seen here was large enough to be seen in a simpler analysis starting with a monthly mean climatological profile. The main reason for preferring the individual 6-hourly MERRA profiles as our starting point was to minimize model bias. Our fitted H_2O profile scale factors showed good agreement with the MERRA total H_2O column density (the median scale factor was 1.21, and the interquartile range was 1.06 to 1.43). Having calibrated the MERRA reanalysis at this site with our direct radiometric measurements, the reanalysis could be used as a tool to extend the site characterization over a longer time period back to 1979.

Data availability. The data that support the plots within this paper and other findings of this study are available from the corresponding author upon reasonable request.

Received 18 July 2016; accepted 31 August 2016; published 12 December 2016

References

1. Phillips, T. G. & Keene J. Submillimeter astronomy. *Proc. IEEE* **80,** 1662–1678 (1992).
2. Watson, D. M. Far-infrared spectroscopy and the physics and chemistry of interstellar clouds. *Phys. Scripta* **T11,** 33–47 (1985).
3. Goldsmith, P. F., Yildiz, U. A., Langer, W. D. & Pineda, J. L. Herschel galactic plane survey of [N II] fine structure emission. *Astrophys. J.* **814,** 133 (2015).
4. Goicoechea, J. R. *et al.* Velocity-resolved [C II] emission and [C II]/FIR mapping along Orion with Herschel. *Astrophys. J.* **812,** 75 (2015).
5. Wiedner, M. C. *et al.* First observations with CONDOR, a 1.5 THz heterodyne receiver. *Astron. Astrophys.* **454,** L33–L36 (2006).
6. Hogerheijde, M. R. *et al.* Probable detection of H_2D^+ in the starless core Barnard 68. *Astron. Astrophys.* **454,** L59–L62 (2006).
7. Caselli, P. *et al.* Survey of ortho-H_2D^+ ($1_{1,0} - 1_{1,1}$) in dense cloud cores. *Astron. Astrophys.* **492,** 703–718 (2008).
8. Rolffs, R. *et al.* Reversal of infall in SgrB2(M) revealed by Herschel/HIFI observations of HCN lines at THz frequencies. *Astron. Astrophys.* **521,** L46 (2010).
9. Harries, J. *et al.* The far-infrared Earth. *Rev. Geophys.* **46,** RG4004 (2008).
10. Yang, H. *et al.* Exceptional terahertz transparency and stability above Dome A, Antarctica. *Publ. Astron. Soc. Pacif.* **122,** 490–494 (2010).
11. J. Qiu China aims high from the bottom of the world. *Nature News* (29 August 2012); http://go.nature.com/2fQfBkN.
12. Li, X.-X. *et al.* A Fourier transform spectrometer for site testing at Dome A. *Proc. SPIE* **7385,** 73851D (2009).
13. Matsushita, S., Matsuo, H., Pardo, J. R. & Radford S. J. E. FTS measurements of submillimeter-wave atmospheric opacity at Pampa la Bola II: supra-terahertz windows and model fitting. *Publ. Astron. Soc. Jpn* **51,** 603–610 (1999).
14. Marrone, D. P. *et al.* Observations in the 1.3 and 1.5 THz atmospheric windows with the Receiver Lab Telescope. In *Proc. 16th Int. Symp. Space Terahertz Technology* (ed Ingvarson, M.) 64–67 (International Symposium on Space Terahertz Technology, 2005).
15. Shine, K. P., Ptashnik, I. V. & Rädel, G. The water vapor continuum: brief history and recent developments. *Surv. Geophys.* **33,** 535–555 (2012).
16. Mlawer, E. J. *et al.* Development and recent evaluation of the MT_CKD model of continuum absorption. *Phil. Trans. R. Soc. A* **370,** 2520–2556 (2012).
17. Ramanathan, V. & Coakley, J. A. Climate modelling through radiative-convective models. *Rev. Geophys. Space Phys.* **16,** 465–489 (1978).
18. Clough, S. A., Iacono, M. & Moncet, J.-L. Line-by-line calculations of atmospheric fluxes and cooling rates: application to water vapor. *J. Geophys. Res.* **97,** 15761–15785 (1992).
19. Turner, D. D., Merrelli, A., Vimont, D. & Mlawer, E. J. Impact of modifying the longwave water vapor continuum absorption model on community Earth system model simulations. *J. Geophys. Res.* **117,** D04106 (2012).
20. Paynter, D. J. & Ramaswamy, V. An assessment of recent water vapour continuum measurements upon longwave and shortwave radiative transfer. *J. Geophys. Res.* **116,** D20302 (2011).
21. Turner, D. D. & Mlawer, E. J. The radiative heating in underexplored bands campaigns. *Bull. Am. Meteorol. Soc.* **91,** 911–923 (2010).
22. Delamere, J. S. *et al.* A far-infrared radiative closure study in the Arctic: application to water vapour. *J. Geophys. Res.* **115,** D17106 (2010).
23. Turner, D. D. *et al.* Ground-based high spectral resolution observations of the entire terrestrial spectrum under extremely dry conditions. *Geophys. Res. Lett.* **39,** L10801 (2012).
24. Bhawar, R. *et al.* Spectrally resolved observations of atmospheric emitted radiance in the H_2O rotation band. *Geophys. Res. Lett.* **35,** L04812 (2008).
25. Serio, C. *et al.* Retrieval of foreign-broadened water vapor continuum coefficients from emitted spectral radiance in the H_2O rotational band from 240 to 590 cm^{-1}. *Opt. Express* **16,** 15816–15833 (2008).
26. Green, P. D. *et al.* Recent advances in measurement of the water vapour continuum in the far-infrared spectral region. *Phil. Trans. R. Soc. A* **370,** 2637–2655 (2012).
27. Rienecker, M. M. *et al.* MERRA: NASA's modern-era retrospective analysis for research and applications. *J. Clim.* **24,** 3624–3648 (2011).
28. Wang, J. *et al.* Unprecedented upper-air dropsonde observations over Antarctica from the 2010 Concordiasi experiment: validation of satellite-retrieved temperature profiles. *Geophys. Res. Lett.* **40,** 1231–1236 (2013).
29. Hudson, S. R. & Brandt, R. E. A Look at the surface-based temperature inversion on the Antarctic plateau. *J. Clim.* **18,** 1673–1696 (2005).
30. Paine, S. The *am* atmospheric model v. 9.0 Submillimeter Array Technical Memo No. 152 (Smithsonian Astrophysical Observatory, 2016); http://doi.org/10.5281/zenodo.61127
31. Martin D. H. & Puplett, E. Polarised interferometric spectrometry for the millimetre and submillimetre spectrum. *Infrared Phys.* **10,** 105–109 (1969).
32. Lawrence, J. S. *et al.* The PLATO Dome A site-testing observatory: power generation and control systems. *Rev. Sci. Instrum.* **80,** 064501 (2009).
33. Revercomb, H. E. *et al.* Radiometric calibration of IR Fourier transform spectrometers: solution to a problem with the high-resolution interferometer sounder. *Appl. Optics* **27,** 3210–3218 (1988).
34. Fleming, J. W. *et al.* Temperature effects and the observation of the B_{2u} lattice mode in the far infrared absorption spectrum of polyethylene. *Chem. Phys. Lett.* **17,** 84–85 (1972).

35. Amrhein, E. M. & Heil, H. Dielectric absorption of polymers from the millimetre to the far infrared region. *J. Phys. Chem. Solids* **32,** 1925–1933 (1971).
36. Chantry, G. W. *et al.* Far infrared and millimetre-wave absorption spectra of some low-loss polymers. *Chem. Phys. Lett.* **10,** 473–477 (1971).

Acknowledgements

We acknowledge the assistance of the 26th and 27th CHINARE teams supported by the Polar Research Institute of China and the Chinese Arctic and Antarctic Administration, the University of New South Wales PLATO team, the CAS Center for Antarctic Astronomy team and the other teams contributing to the operation of the Dome A facilities, in particular J.W.V. Storey, D.M. Luong-Van, A. Moore, C. Pennypacker, D. York, L. Wang, L. Feng, Z. Zhu, H. Yang, X. Cui, X. Yuan, X. Gong, X. Zhou, X. Liu, Z. Wang, and J. Huang. The exemplary work of D. Naylor and B. Gom of Blue Sky Spectroscopy Inc. and K. Wood of QMC Instruments Inc. is acknowledged. We also acknowledge discussions with D.D. Turner of NOAA on complex-domain calibration of the FTS spectra, and E.J. Mlawer of AER Inc. on the MT_CKD water vapour continuum model and its implementation in the radiative transfer code used in this work. MERRA data used in this study were provided by the Global Modeling and Assimilation Office (GMAO) at NASA Goddard Space Flight Center through the NASA GES DISC online archive. Primary support for this research was provided by the Operation, Maintenance and Upgrading Fund for Astronomical Telescopes and Facility Instruments, funded by the Ministry of Finance of China (MOF) and administered by the CAS. The traverse team was financially supported by the Chinese Polar Environment Comprehensive Investigation & Assessment Program. The PLATO team was funded by the Australian Research Council and the Australian Antarctic Division. Iridium satellite communications were provided by the US National Science Foundation and the US Antarctic Program. Co-authors S.P. and Q.Z. received additional support for this work from Smithsonian Institution Endowment funds and the Smithsonian Competitive Grants Program for Science. Co-author H.M. was supported partly by a visiting professorship of CAS for senior international scientists.

Author contributions

S.-C.S., S.P., Q.Z. and J.Y. proposed the Dome A FTS project, with S.-C.S. as the principal investigator. All authors contributed substantially to multiple aspects of the work presented here. All authors commented upon and approved the final manuscript.

Additional information

Supplementary information is available for this paper.

Reprints and permissions information is available at www.nature.com/reprints.

Correspondence and requests for materials should be addressed to S.C.S.

How to cite this article: Shi, C.-S. *et al.* Terahertz and far-infrared windows opened at Dome A in Antarctica. *Nat. Astron.* **1,** 0001 (2016).

Competing interests

The authors declare no competing financial interests.